Supplementary Information

Ionic Atmosphere and Temperature - Field - Promoted Dissociation and Phase Reconstruction of Bastnasite

Qionghua Xie [a,b,c,d,e], Yifan Hao [a,c,d,e], Guocheng Yao [a,c,d,e], Cong Wang [b], Liangshi Wang [*a,c,d,e]

[a] National Engineering Research Center for Environment-friendly Metallurgy in Producing Premium Non-ferrous Metals, China GRINM Group Co., Ltd., Beijing 101407, China.

[b] School of Metallurgy, Northeastern University, Shenyang, Liaoning 110819, China.

[c] Beijing Engineering Research Center of Strategic Nonferrous Metals Green Manufacturing Technology, GRINM Resources and Environment Tech. Co., Ltd., Beijing 101407, China.

[d] General Research Institute for Nonferrous Metals, Beijing 100088, China.

[e] GRIMAT Engineering Institute Co., Ltd., Beijing 101407, China.

*Corresponding author. E-mail address: wangliangshi@grinm.com (L. Wang)

This PDF file includes:

S1 Thermodynamic data of Ce-Cl-F-H_2O system

Based on the Gibbs free energy (ΔG) data obtained using HSC Chemistry 6.0 software, the electrode potentials (E) for each reaction in the corresponding system were calculated using the Nernst equation. This data was used to construct an Eh-pH diagram for the Ce-Cl-F-H_2O system. The Eh-pH diagram illustrates the thermodynamic stability regions of the rare earth multi-component system on the pH and Eh scales. Using the standard hydrogen electrode (SHE) as a reference, this study only considers ideal solutions. The general equations and equilibrium potential expressions for chemical reactions in aqueous solutions are shown in Equations (1) and (2):

$$aA + nH^+ + ze = bB + cH_2O \quad (1)$$

a, n, b and c are the stoichiometric coefficients of each component in the reaction formula. Z is the number of electrons participating in the reaction.

$$E = E^{\Theta} + \frac{2.303RT}{zF} lg\left(\frac{a_A^a}{a_B^b}\right) - \frac{2.303RT}{zF} n \cdot pH \quad (2)$$

The equilibrium potential was calculated using the above equation, and an Eh-pH diagram was plotted.

The Gibbs free energy values (ΔG) of the substances involved in the Ce-Cl-F-H_2O system are shown in Table S1, with the concentrations of Ce, Cl, and F fixed at 1 mol/kg H_2O.

Table S1 ΔG^{θ} of each species in the Ce-Cl-F-H_2O system at different temperatures

Specie	ΔG^{θ}, 293k (kJ/mol)	ΔG^{θ},,323k (kJ/mol)	ΔG^{θ},,348k (kJ/mol)	ΔG^{θ}, 368k (kJ/mol)
$H_2O(l)$	-237.961	-233.091	-229.103	-225.953
F^-	-282.600	-277.072	-272.190	-268.120
HF	-300.068	-297.676	-295.618	-293.932
Cl^-	-131.855	-128.105	-124.675	-121.746
Cl_2	6.435	9.493	11.995	13.943
HCl	-128.030	-123.210	-119.372	-116.409
Ce	0.000	0.000	0.000	0.000
Ce^{3+}	-677.394	-674.881	-672.460	-670.334
Ce^{4+}	-509.620	-502.841	-497.239	-492.756
CeO_2	-1028.164	-1021.800	-1016.512	-1012.291
Ce_2O_3	-1723.601	-1716.176	-1708.792	-1702.912
$Ce(OH)_3$	-1281.099[1]	/	/	/
$Ce(OH)_2^{2+}$	-940.400	-932.100	-925.068	-920.868
$CeCl_3 \cdot 7H_2O$	-2700.161	-2651.356	-2609.864	-2576.169
$CeCl_3$(aq)	-1070.886	-1058.779	-1048.070	-1039.167
CeClO	-952.839	-946.974	-941.959	-937.869
$CeCl_2^+$	-940.923	-933.364	-926.860	-799.826
$CeCl^{2+}$	-810.842	-806.517	-802.829	-799.826
$CeCl_4^-$	-1200.707	-1182.648	-1166.244	-1152.369
CeF_3^+	-1470.331[2, 3]	/	/	/
CeF_2^{2+}	-1156.151[2, 3]	/	/	/
CeF^{3+}	-834.680[2, 3]	/	/	/
CeF_4	-1755.456	-1745.874	-1737.946	-1731.636

Note: '/' indicates that no data can be found at that temperature.

S2 DFT calculation

Density functional theory (DFT) calculations were performed with ORCA 5.0.3 software package[4]. DFT calculations were carried out with the PBE0 functional with the combination of the Grimme's D3BJ version of dispersion correction[5]. The basis set of def2-SVP for F and effective core potential SDD for Ce and Pr were adopt the geometry optimization and frequency calculations. Single-point energy calculations using the def2-TZVP basis set on the above basis. The geometries were fully optimized without any structural constraints. The harmonic frequency calculations were carried out at the same level of theory to verify that all structures have no imaginary frequency. The implicit solvation model SMD with water as the solvent was applied in the calculations. The molecular structure and properties were analyzed and visualized using Multiwfn [6]. The electrostatic

potential (ESP) [7, 8], average local ionization energy (ALIE) [9], orbital-weighted Fukui function, and orbital-weighted double descriptor (DD) involved in the analysis were evaluated by the efficient algorithm proposed in Multiwfn [10].

S3 Distinct Electronic Structures and Coordination Behaviors of Cerium and Praseodymium

Given the similar properties of REEs, high-value REEs (e.g., Pr) inevitably complex with F^- during coordination leaching-CeF_3 precipitation of bastnaesite, potentially causing Pr loss and reduced CeF_3 purity. Clarifying intrinsic Ce and Pr property disparities is crucial for controlling high-value REEs behavior. DFT-calculated energy levels and orbital distributions (Fig. 3(g)), ionization energies and electron affinities (Fig. 3(h)), and $[PrF_x]^{4-x}$ binding energies (Fig. 3(i)) reveal greater electron stability of Ce^{4+}/ Pr^{4+} versus Ce^{3+}/Pr^{3+}, with Ce^{4+} exceeding Pr^{4+} stability - consistent with observed refractory leaching of high-valence REEs phases. In F^--rich solutions, both Ce^{4+} and Pr^{4+} readily complex with F^-. Although $[PrF_x]^{4-x}$ exhibits higher binding energy than $[CeF_x]^{4-x}$, yet distinct orbital configurations yield markedly different structures. Unlike the stable linear diatomic and triangular triatomic forms of $[CeF_x]^{4-x}$, $[PrF_x]^{4-x}$ displays suboptimal linear diatomic and planar T-shaped triatomic configurations, reducing spatial stability. Pr^{3+}'s smaller ionic radius, denser lattice, and higher reactivity impart lower PrF_3 binding energy versus CeF_3 (Fig. S1). However, minimal energy differences permit strategic aging control to suppress high-value praseodymium fluoride deposition when [Pr]≪[Ce]. Concurrently, higher binding energies of $[CeF_3]^+$/$[PrF_3]^+$ versus CeF_3/PrF_3 confirm F^-'s preference for tetravalent REE coordination during leaching.

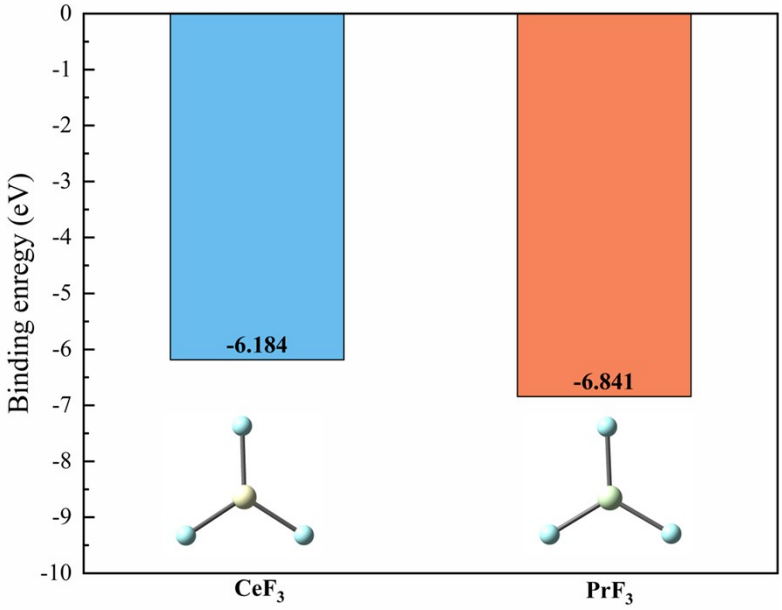

Fig S1 The binding energy of CeF_3 and PrF_3

S4 Fluoride ion concentration in leachate from different leaching systems

Table S2 Fluoride ion concentration in leachate from different leaching systems

Leaching system	F^- (mg/L)
2 mol/L HCl	7.58
2 mol/L HCl+5w% H_2SO_4	385.36
4 mol/L HCl	185.76
4 mol/L HCl+5w% H_2SO_4	5665.24

S5 Molecular dynamics simulation

The molecular dynamics simulations were performed using the GROMACS software package (version 2021.3) [11-14]. The initial system was constructed using PACKMOL [15], comprising specific molecules solvated in a cubic box with an edge size of 5 nm. The TIP3P water model was employed to solvate the system. Periodic boundary conditions were applied in all three spatial directions. Atomic interactions were parameterized using the Generalized Amber Force Field (GAFF) [16], and atomic charges were assigned based on RESP2 charges derived from Multiwfn [17]. Following energy minimization, the system was equilibrated in the NPT ensemble. The Berendsen barostat was used for pressure coupling during a 1 ns pre-equilibration stage. Subsequently, a production simulation was conducted in the NPT ensemble for a total duration of 20 ns at temperatures of 298 K and 363 K, using a time step of 1 fs. During the production run, the temperature was controlled by the V-rescale thermostat (τT = 1 ps) and the pressure was maintained using the Parrinello-Rahman

barostat (τP = 2 ps). The convergence and stability of the simulations were assessed by monitoring the evolution of potential energy, temperature, pressure, and density over time. The system was considered equilibrated and stable once these properties reached a steady state with minimal fluctuations. Finally, radial distribution functions (RDF) and mean squared displacements (MSD) of the particles were analyzed using the built-in tools in GROMACS.

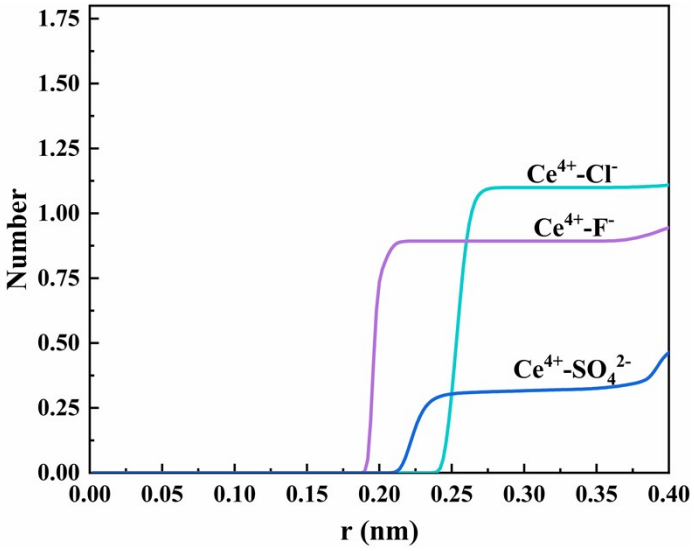

Fig. S2 Calculated molecular dynamics of coordination leaching of the Ce^{4+}-Cl^- -F^--SO_4^{2-} system: coordination number

S6 Changes in the deposition process of immersion liquid under different temperature fields

At ambient temperature (Fig. S3(a)), the leachate gradually became turbid within 1 h. At 1.5 h, a distinct precipitated layer appeared within the system. This occurs because, as the standing time increases, the abundant Cl^- present in the system continuously reduces Ce^{4+}, destabilizing the $[CeF_x]^{4-x}$ complexes. Subsequently, the liberated RE^{3+} and F^- ions gradually aggregate due to their strong ionic interactions, forming small solid particles (nuclei) that cause turbidity in the deposition solution. As these nuclei further grow and aggregate, they gradually settle to the bottom of the beaker. With prolonged aging time, the transparency of the deposition solution increases, the amount of precipitate gradually rises, and the initially dense deposited layer transforms into an accumulated deposited layer.

Under high temperature (Fig. S3(b)), the deposition solution is heated, accelerating the formation and growth of rare earth fluoride nuclei. This causes the upper liquid layer to become turbid first. Simultaneously, the solid particles gradually descend to the bottom of the beaker, forming a thick deposited layer. As the aging time extends, the thickness of the deposited layer decreases, and the transparency of the deposition solution increases.

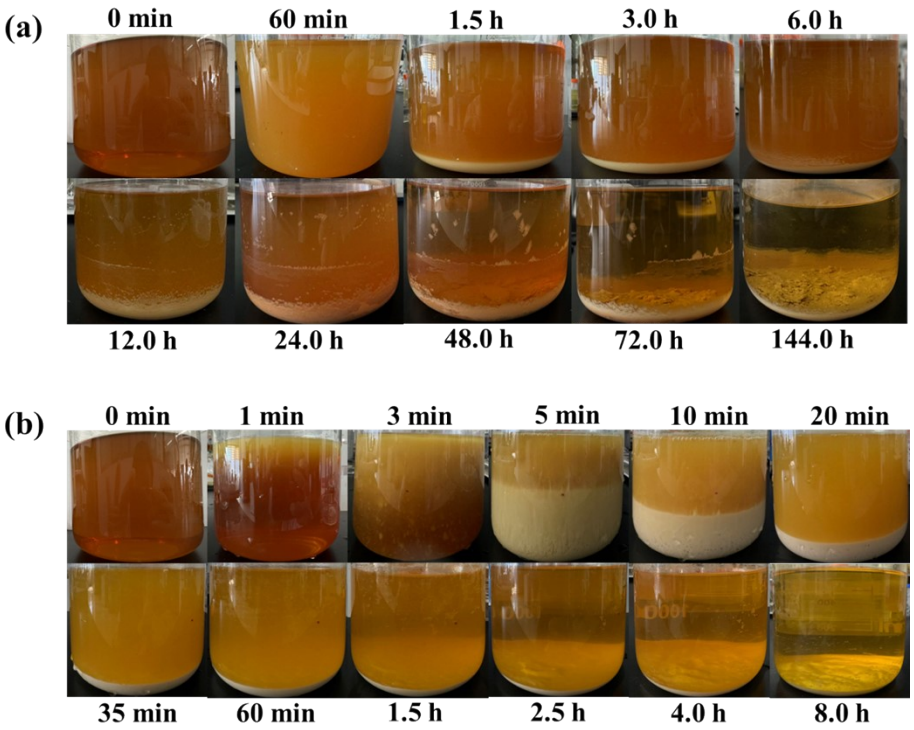

Fig S3 Changes in the deposition process of immersion liquid under different temperature fields: (a) Room temperature (25 °C); (b) High temperature (90 °C)

S7 The composition and morphology of sediments obtained by different temperature fields and aging time

Table S3 The composition (content (wt%)) of the sediments obtained after aging at 25°C for different time

Component	1.5 h	3 h	6 h	12 h	24 h	48 h	72 h	144 h
CeO_2	37.63	40.20	31.01	32.70	53.16	42.92	37.76	39.29
La_2O_3	14.35	15.22	8.93	8.67	10.51	7.04	8.53	13.98
Nd_2O_3	2.69	3.07	1.93	2.30	3.41	2.96	2.79	3.00
F	15.23	22.96	27.43	34.83	20.08	27.76	33.16	24.14
SO_3	6.25	7.26	2.23	3.98	4.44	3.91	3.57	7.73
CO_2	15.71	4.97	25.61	15.07	5.48	13.23	11.98	7.90
Cl	3.30	1.69	0.42	0.19	0.45	0.76	0.66	1.79
SrO	1.86	1.71	0.89	0.82	0.88	0.41	0.55	0.75
CaO	1.79	1.77	1.04	0.95	1.07	0.82	0.77	1.22
ThO_2	1.00	1.00	0.48	0.43	0.46	0.20	0.23	0.20
K_2O	0.20	0.16	0.04	0.07	0.07	0.00	0.00	0.00
Rare earth distribution	1.5 h	3 h	6 h	12 h	24 h	48 h	72 h	144 h
CeO_2	68.83	68.73	74.05	74.88	79.26	81.12	76.94	69.82
La_2O_3	26.26	26.02	21.34	19.86	15.66	13.30	17.38	24.85
Nd_2O_3	4.91	5.25	4.62	5.26	5.08	5.58	5.68	5.34

Table S4 The composition (content (wt%)) of the sediments obtained after aging at 90°C for different time.

Component	5 min	10 min	20 min	35 min	60 min	1.5 h	2.5 h	4 h	8 h
CeO_2	30.52	32.58	30.89	35.43	34.93	30.41	34.24	28.52	26.57
La_2O_3	13.10	17.91	15.48	15.56	18.52	17.14	17.72	16.01	15.24
Pr_6O_{11}	7.69	0.51	0.42	0.73	0.64	0.52	0.64	0.58	0.43
Nd_2O_3	2.63	3.90	3.28	3.65	4.10	4.00	4.38	3.57	3.45
F	16.47	17.28	24.32	16.65	12.94	21.67	13.08	17.47	24.06
SO_3	3.58	9.20	10.50	9.60	11.27	11.33	10.98	7.88	7.04
CO_2	18.60	12.77	9.10	11.06	10.66	9.12	12.02	19.41	17.34
Cl	3.91	3.24	3.60	2.93	4.12	3.29	3.96	4.31	3.65
SrO	0.82	0.52	0.47	0.91	0.53	0.47	0.56	0.44	0.40
CaO	1.33	1.28	1.17	1.52	1.39	1.39	1.40	1.24	1.19
Fe_2O_3	0.85	0.60	0.60	1.51	0.67	0.46	0.77	0.37	0.46
ThO_2	0.50	0.22	0.18	0.47	0.24	0.20	0.25	0.21	0.18
Rare earth distribution	5 min	10 min	20 min	35 min	60 min	1.5 h	2.5 h	4 h	8 h
CeO_2	56.57	59.34	61.70	63.99	60.04	58.40	60.09	58.58	58.15
La_2O_3	24.29	32.62	30.91	28.11	31.83	32.92	31.09	32.89	33.35
Pr_6O_{11}	14.26	0.93	0.83	1.31	1.09	0.99	1.12	1.19	0.94
Nd_2O_3	4.88	7.11	6.56	6.59	7.04	7.69	7.69	7.34	7.56

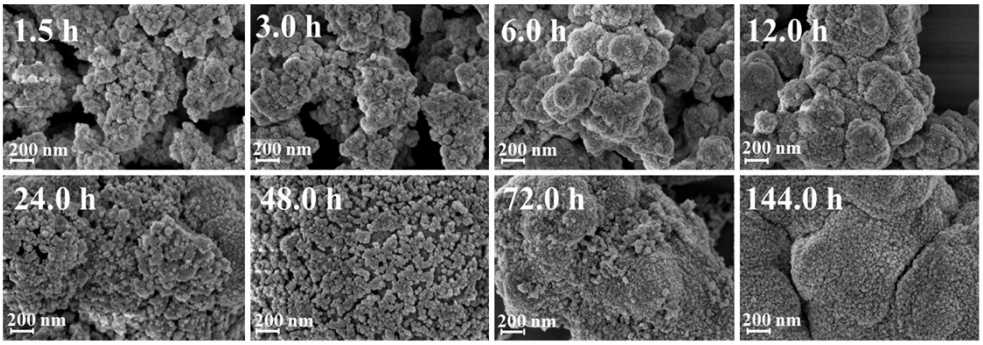

Fig. S4 SEM morphology (200 nm) of sediments obtained by aging for different times in the temperature field at room temperature (25 °C)

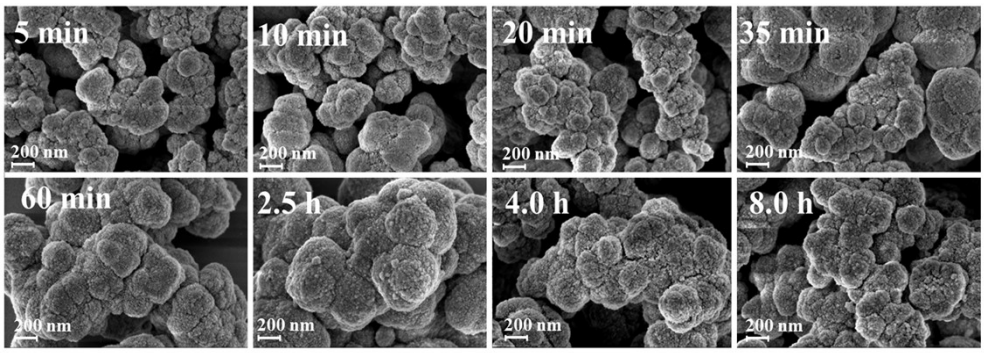

Fig. S5 SEM morphology (200 nm) of sediments obtained by aging for different times in the temperature field at high temperature (90 °C)

S8 Ion diffusion coefficients at different temperatures

Analysis of ion diffusion coefficients at different temperatures (Fig. 8(c,f)) reveals that at 25 °C, the diffusion rates of Ce^{4+} and SO_4^{2-} are essentially identical, indicating a relatively stable ionic atmosphere. Concurrently, the difference in diffusion coefficients between Ce^{4+} and Pr^{3+} is relatively large at 25 °C, hindering their co-deposition. The diffusion coefficients of Ce^{4+} and Cl^- exhibit significant temperature sensitivity. The high-temperature field markedly accelerates their diffusion rates, leading to a faster precipitation rate of CeF_3. Meanwhile, the difference in diffusion coefficients between Ce^{4+} and Pr^{3+} diminishes at elevated temperatures, facilitating the co-deposition of Pr^{3+}.

References

1. S. A. Hayes, P. Yu, T. J. O'Keefe, M. J. O'Keefe and J. O. Stoffer, *J. Electrochem. Soc.*, 2002, **149**, C623.
2. N. K. Chaudhuri, R. M. Sawant and K. L. Ramakumar, *Rev. Inorg. Chem.*, 2001, **21**, 331-368.
3. G. Shuai, L. Zhao, L. Wang, Z. Long and D. Cui, *J. Rare Earths*, 2017, **35**, 1255-1260.
4. E. C. (A) C. Bannwarth, S. Ehlert, A. Hansen, P. Pracht, J. Seibert, S. Spicher, S. Grimme WIREs Comput. Mol. Sci., 2020, 11, e01493. (B) S. Grimme, C. Bannwarth, P. Shushkov, J. Chem. Theory Comput., 2017, 13, 1989-2009. (C) C. Bannwarth, S. Ehlert and S. Grimme., J. Chem. Theory Comput., 2019, 15, 1652-1671. (D) P. Pracht, E. Caldeweyher, S. Ehlert, S. Grimme, ChemRxiv, 2019, preprint.
5. S. Grimme, J. Antony, S. Ehrlich and H. Krieg, *J. Chem. Phys.*, 2010, **132**, 154104.
6. T. Lu and F. W. Chen, *J. Comput. Chem.*, 2012, **33**, 580-592.
7. T. Lu and F. W. Chen, *J. Mol. Graphics Modell.*, 2012, **38**, 314-323.
8. J. Zhang and T. Lu, *Phys. Chem. Chem. Phys.*, 2021, **23**, 20323-20328.
9. P. Sjoberg, J. S. Murray, T. Brinck and P. Politzer, *Canadian Journal of Chemistry*, 1990, **68**, 1440-1443.
10. T. Lu and Q. X. Chen, in *Conceptual Density Functional Theory*, 2022, DOI: 10.1002/9783527829941.ch31, pp. 631-647.
11. D. Van Der Spoel, E. Lindahl, B. Hess, G. Groenhof, A. E. Mark and H. J. C. Berendsen, *J. Comput. Chem.*, 2005, **26**, 1701-1718.
12. S. Páll, M. J. Abraham, C. Kutzner, B. Hess and E. Lindahl, Cham, 2015.
13. M. J. Abraham, T. Murtola, R. Schulz, S. Páll, J. C. Smith, B. Hess and E. Lindahl, *SoftwareX*, 2015, **1-2**, 19-25.
14. H. J. C. Berendsen, D. van der Spoel and R. van Drunen, *Comput. Phys. Commun.*, 1995, **91**, 43-56.
15. L. Martínez, R. Andrade, E. G. Birgin and J. M. Martínez, *J. Comput. Chem.*, 2009, **30**, 2157-2164.
16. J. Wang, R. M. Wolf, J. W. Caldwell, P. A. Kollman and D. A. Case, *J. Comput. Chem.*, 2004, **25**, 1157-1174.
17. T. Lu and F. Chen, *J. Comput. Chem.*, 2012, **33**, 580-592.